Filtered backprojection proton CT reconstruction along most likely paths

Simon Rit,[a] George Dedes, Nicolas Freud, David Sarrut, and Jean Michel Létang
Université de Lyon, CREATIS, CNRS UMR5220, Inserm U1044, INSA-Lyon, Université Lyon 1, Centre Léon Bérard, 69008 Lyon, France

(Received 28 July 2012; revised 7 October 2012; accepted for publication 11 October 2012; published 28 February 2013)

Purpose: Proton CT (pCT) has the potential to accurately measure the electron density map of tissues at low doses but the spatial resolution is prohibitive if the curved paths of protons in matter is not accounted for. The authors propose to account for an estimate of the most likely path of protons in a filtered backprojection (FBP) reconstruction algorithm.
Methods: The energy loss of protons is first binned in several proton radiographs at different distances to the proton source to exploit the depth-dependency of the estimate of the most likely path. This process is named the distance-driven binning. A voxel-specific backprojection is then used to select the adequate radiograph in the distance-driven binning in order to propagate in the pCT image the best achievable spatial resolution in proton radiographs. The improvement in spatial resolution is demonstrated using Monte Carlo simulations of resolution phantoms.
Results: The spatial resolution in the distance-driven binning depended on the distance of the objects from the source and was optimal in the binned radiograph corresponding to that distance. The spatial resolution in the reconstructed pCT images decreased with the depth in the scanned object but it was always better than previous FBP algorithms assuming straight line paths. In a water cylinder with 20 cm diameter, the observed range of spatial resolutions was $0.7 - 1.6$ mm compared to $1.0 - 2.4$ mm at best with a straight line path assumption. The improvement was strongly enhanced in shorter 200° scans.
Conclusions: Improved spatial resolution was obtained in pCT images with filtered backprojection reconstruction using most likely path estimates of protons. The improvement in spatial resolution combined with the practicality of FBP algorithms compared to iterative reconstruction algorithms makes this new algorithm a candidate of choice for clinical pCT. © *2013 American Association of Physicists in Medicine*. [http://dx.doi.org/10.1118/1.4789589]

Key words: proton computed tomography, proton CT, filtered backprojection, most likely path

I. INTRODUCTION

Proton computed tomography (pCT) has been considered very early in the history of CT (Ref. 1) with a continuous development until the beginning of the 1980s. Its investigation was then slowed down because the ratio between benefits and cost was too low compared to photon CT scanners but the development of proton therapy has triggered new studies on pCT scanners.[2–4]

pCT could indeed improve proton therapy compared to current clinical practice since it could reduce the uncertainty of the proton therapy planning due to the lack of accuracy in the proton stopping power of tissues computed from photon CT images.[5,6] This uncertainty contributes to the range uncertainty margin which is between 2.5% + 1 mm and 3.5% + 3 mm depending on the hospital.[7] It would be reduced with pCT since the proton stopping power is better characterized with protons than photons. Another potential benefit is the reduction of the imaging dose compared to photon CT (Refs. 8 and 9) since the energy loss of every proton can be measured and provides information about the patient tissues, while measurement of the probability of interactions of photons with tissues requires a large number of photons. Finally, pCT is an additional modality which could have its own advantages for improving the diagnostic.[10]

pCT has one major drawback compared to photon CT, its lack of spatial resolution. Indeed, protons traversing matter undergo multiple deflections due to multiple Coulomb scattering, resulting in curved trajectories and blurred proton radiographs.[11] Many research initiatives of the past decade have focused on this issue and it has been proposed to track each proton individually using pairs of position-sensitive detectors before and after the scanned object.[3,4,12] The measured positions are used to estimate the most likely path of each individual proton which has proven efficient to improve spatial resolution using Monte Carlo simulations.[9,13–15]

The estimation of the most likely path of each proton resolves in a curve. The pCT reconstruction problem, therefore, relates to the inversion of the generalized Radon transform where one integrates the sought pCT image over a family of curves. This problem has already been studied in motion-compensated CT reconstruction.[16] There is still no exact analytical inversion for curved lines, it is only known how to compensate for a motion that preserves the straightness of integration lines.[17] However, approximate algorithms based

on voxel-specific backprojection have proven efficient to increase spatial resolution.[18,19]

Most likely paths have only been used in pCT reconstruction algorithms to select the protons having straight trajectories in a filtered backprojection (FBP) algorithm[8] or in iterative reconstruction algorithms.[20,21] However, FBP algorithms with most likely paths would be desirable in clinical practice to improve spatial resolution with a practical algorithm, similar to what has been developed for motion-compensated CT.[22] In this paper, we propose a practical FBP algorithm for pCT reconstruction using the curved most likely path of each proton based on voxel-specific backprojections with an intermediate binning step to handle the acquired list-mode data.

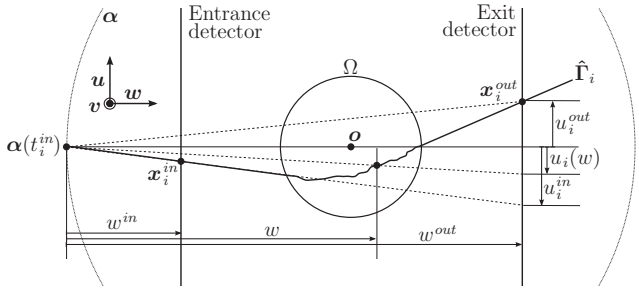

FIG. 1. Schematic top view of the pCT scanner used in this study. The signed distances w^{out}, w^{in}, w and u_i^{out}, u_i^{in}, $u_i(w)$ are used in Eqs. (6)– (8), respectively. The effect of multiple Coulomb scattering in the object has purposely been exaggerated for the sake of the clarity of the scheme.

II. METHOD

II.A. pCT reconstruction problem

Protons lose most of their energy via electromagnetic inelastic collisions if they do not undergo nuclear interactions. The local energy loss $\mathrm{d}E$ at a point of space $\boldsymbol{x} \in \mathbb{R}^3$ is given by

$$-\frac{\mathrm{d}E}{\mathrm{d}x}(\boldsymbol{x}) = \eta(\boldsymbol{x})S(I(\boldsymbol{x}), E(\boldsymbol{x})), \tag{1}$$

where $\eta : \mathbb{R}^3 \to \mathbb{R}$ is the relative electron density with respect to a reference medium (water in this study), $S : \mathbb{R}^2 \to \mathbb{R}$ is the proton stopping power in the reference medium given by the Bethe-Bloch equation[23] which, under realistic simplifications,[24] only depends on $I : \mathbb{R}^3 \to \mathbb{R}$, the tissue-specific ionization potential, and $E : \mathbb{R}^3 \to \mathbb{R}$, the energy of the proton crossing the tissue. The ionization potential I varies moderately in human tissues and has a limited effect on S so, in pCT, it is typically approximated to that of water, i.e., $I(\boldsymbol{x}) = I_{\text{water}} = 78\,\text{eV},\ \forall \boldsymbol{x} \in \mathbb{R}^3$ in our simulations. Under this assumption, integrating Eq. (1) leads to the line integral

$$\int_{\boldsymbol{\Gamma}_i} \eta(\boldsymbol{x})\mathrm{d}l = \int_{E_i^{out}}^{E_i^{in}} \frac{\mathrm{d}E}{S(I_{\text{water}}, E)} \tag{2}$$

with $i \in \mathbf{I} \subset \mathbb{N}$ the index of tracked protons, $\boldsymbol{\Gamma}_i(t) \in \mathbb{R}^3$ the curved trajectory of the proton, function of time $t \in \mathbb{R}$, and E_i^{in} and E_i^{out} the energies of the proton at the entrance and exit detectors. Finding η from E_i^{in}, E_i^{out} and an estimate $\hat{\boldsymbol{\Gamma}}_i(t) \in \mathbb{R}^3$ of the path $\boldsymbol{\Gamma}_i$ for a set $\mathbf{I}$ of protons is the pCT reconstruction problem.

The energy integral is defined as $G : \mathbb{R}^2 \to \mathbb{R}$ to simplify notations in the following with

$$G(E_i^{in}, E_i^{out}) = \int_{E_i^{out}}^{E_i^{in}} \frac{\mathrm{d}E}{S(I_{\text{water}}, E)}. \tag{3}$$

In practice, the incident energy E_i^{in} of a monoenergetic proton beam would be assumed to be known, the exit energy could be measured with, e.g., a calorimeter detector, and the energy loss in air would be neglected.

II.B. pCT scanner for most likely path estimation

Proton path estimation is a crucial problem in pCT reconstruction because it directly influences the spatial resolution.[11] Several solutions have been proposed to the problem of most likely path (MLP) estimation.[9,13,14] These recent works on MLP estimation rely on pCT scanners[3,4] which are able to track the position and the direction of each proton, before and after traversing the object.

We assumed a similar cone-beam pCT scanner in this study with a proton source following a circular trajectory $\boldsymbol{\alpha}(t) \in \mathbb{R}^3$ around the axis defined by the isocenter $\boldsymbol{o} \in \mathbb{R}^3$ and the unit axis $\boldsymbol{v} \in \mathbb{R}^3$ (Fig. 1). 2D tracking detectors were positioned before and after the scanned object to record the entrance and exit positions and directions of each proton noted

$$\begin{cases} \boldsymbol{x}_i^{in} &= \boldsymbol{\Gamma}_i(t_i^{in}) \\ \boldsymbol{x}_i^{out} &= \boldsymbol{\Gamma}_i(t_i^{out}) \\ \dot{\boldsymbol{x}}_i^{in} &= \dfrac{\mathrm{d}\boldsymbol{\Gamma}_i(t_i^{in})}{\mathrm{d}t} \\ \dot{\boldsymbol{x}}_i^{out} &= \dfrac{\mathrm{d}\boldsymbol{\Gamma}_i(t_i^{out})}{\mathrm{d}t} \end{cases} \tag{4}$$

with $t_i^{in}, t_i^{out} \in \mathbb{R}$ the times at which proton i crosses the entrance and exit tracking detectors, respectively. We define the unit vectors $\boldsymbol{u}, \boldsymbol{w} : \mathbb{R}^3 \to \mathbb{R}^3$ depending on the source position, with $\boldsymbol{w}(\boldsymbol{\alpha}(t)) = -\boldsymbol{\alpha}(t)/\|\boldsymbol{\alpha}(t)\|_2$ and $\boldsymbol{u}(\boldsymbol{\alpha}(t)) = \boldsymbol{v} \times \boldsymbol{w}(\boldsymbol{\alpha}(t))$ to dispose of a 3D Cartesian coordinate system $\{\boldsymbol{u}, \boldsymbol{v}, \boldsymbol{w}\}$ in the frame of reference of the source/detector pair. $\boldsymbol{u}$ and $\boldsymbol{v}$ therefore define the orientation of the detectors and $\boldsymbol{w}$ the main beam direction. We also assumed that the convex hull of the object $\Omega \subset \mathbb{R}^3$ was known which can practically be measured with a surface scanner or an initial reconstruction without MLPs.

The algorithm proposed in this work is applicable to any MLP estimation $\hat{\boldsymbol{\Gamma}}_i$ from the convex hull Ω and the list-mode proton data E_i^{in}, $\boldsymbol{x}_i^{in}$, $\dot{\boldsymbol{x}}_i^{in}$, E_i^{out}, $\boldsymbol{x}_i^{out}$, and $\dot{\boldsymbol{x}}_i^{out}$.

II.C. Distance-driven binning

Our objective is to adapt existing filtered backprojection algorithms for pCT reconstruction. Previous filtered backprojection algorithms for pCT have binned list-mode proton data

in virtual proton radiographs and we recall first this binning process. Let $j \in \mathbf{J} \subset \mathbb{Z}^2$ be a set of spatial indices corresponding to a grid of pixels of the exit tracking detector and $h : \mathbb{R}^2 \to \mathbb{R}$ their indicators,

$$h_j(\boldsymbol{y}) = \begin{cases} 1 & \text{if } \boldsymbol{y} \in \mathbb{R}^2 \text{ is in pixel } j, \\ 0 & \text{else.} \end{cases} \tag{5}$$

It is assumed that the pCT scanner operates in a step-and-shoot mode with gantry rotations only during beam-off time to have, during beam-on times, a discrete number of source positions $\boldsymbol{a}_p \in \mathbb{R}^3$, $p \in \mathbf{P} = \{1, ..., P\}$ with $P \in \mathbb{N}$ the number of source positions. The list-mode proton data are partitioned in subsets $\mathbf{I}_p \subset \mathbf{I}$ of protons emitted from the same source position. We define the binning of list-mode data for each source position in virtual proton radiographs sampled at the exit detector as

$$g_{j,p}^{out} = \frac{\sum_{i \in \mathbf{I}_p} h_j\left(u_i^{out}, v_i^{out}\right) G\left(E_i^{in}, E_i^{out}\right)}{\sum_{i \in \mathbf{I}_p} h_j\left(u_i^{out}, v_i^{out}\right)} \tag{6}$$

with the distances u_i^{out} and v_i^{out} relative to $\boldsymbol{a}_p = \boldsymbol{\alpha}(t_i^{in})$ in the $\{\boldsymbol{u}, \boldsymbol{v}, \boldsymbol{w}\}$ system (Fig. 1),

$$\begin{cases} u_i^{out} = \left(\boldsymbol{x}_i^{out} - \boldsymbol{a}_p\right) \cdot \boldsymbol{u}(\boldsymbol{a}_p), \\ v_i^{out} = \left(\boldsymbol{x}_i^{out} - \boldsymbol{a}_p\right) \cdot \boldsymbol{v}. \end{cases}$$

Repeating this operation for each of the P source positions, one obtains a typical set of P projection images that has already been used in standard filtered-backprojection algorithms for pCT reconstruction assuming a straight proton path between $\boldsymbol{a}_p$ and $\boldsymbol{x}_i^{out}$.[8,24–26]

We observe that this principle can be extended, and we propose to do another binning using the entrance positions $\boldsymbol{x}_i^{in}$ to bin list-mode proton data on the exit detector assuming a straight proton path going through $\boldsymbol{a}_p$ and $\boldsymbol{x}_i^{in}$, i.e.,

$$g_{j,p}^{in} = \frac{\sum_{i \in \mathbf{I}_p} h_j\left(u_i^{in}, v_i^{in}\right) G\left(E_i^{in}, E_i^{out}\right)}{\sum_{i \in \mathbf{I}_p} h_j\left(u_i^{in}, v_i^{in}\right)} \tag{7}$$

with the distances (Fig. 1),

$$\begin{cases} u_i^{in} = \dfrac{w^{out}}{w^{in}}\left(\boldsymbol{x}_i^{in} - \boldsymbol{a}_p\right) \cdot \boldsymbol{u}(\boldsymbol{a}_p), \\ v_i^{in} = \dfrac{w^{out}}{w^{in}}\left(\boldsymbol{x}_i^{in} - \boldsymbol{a}_p\right) \cdot \boldsymbol{v}, \\ w^{in} = \left(\boldsymbol{x}_i^{in} - \boldsymbol{a}_p\right) \cdot \boldsymbol{w}(\boldsymbol{a}_p), \\ w^{out} = \left(\boldsymbol{x}_i^{out} - \boldsymbol{a}_p\right) \cdot \boldsymbol{w}(\boldsymbol{a}_p). \end{cases}$$

The ratio w^{out}/w^{in} is the constant magnification from the entrance to the exit detection plane produced by a cone-beam with apex $\boldsymbol{a}_p$ to obtain the coordinates on the exit flat panel. Therefore, if protons were traveling in straight lines, $g_{j,p}^{in}$ and $g_{j,p}^{out}$ would be equal and their actual differences are due to multiple Coulomb scattering.

We extend the binning to any distance from the source and propose the concept of distance-driven binning, given by

$$g_{j,p}(w) = \frac{\sum_{i \in \mathbf{I}_p} h_j(u_i(w), v_i(w)) G(E_i^{in}, E_i^{out})}{\sum_{i \in \mathbf{I}_p} h_j(u_i(w), v_i(w))} \tag{8}$$

with the distances illustrated in Fig. 1,

$$\begin{cases} u_i(w) = \dfrac{w^{out}}{w}(\hat{\boldsymbol{\Gamma}}_i(t_{i,w}) - \boldsymbol{a}_p) \cdot \boldsymbol{u}(\boldsymbol{a}_p), \\ v_i(w) = \dfrac{w^{out}}{w}(\hat{\boldsymbol{\Gamma}}_i(t_{i,w}) - \boldsymbol{a}_p) \cdot \boldsymbol{v}. \end{cases}$$

Here, $t_{i,w}$ is the time at which proton i crosses the plane parallel to the detectors at distance $w \in \mathbb{R}$ from the source, i.e., $(\hat{\boldsymbol{\Gamma}}_i(t_{i,w}) - \boldsymbol{a}_p) \cdot \boldsymbol{w}(\boldsymbol{a}_p) = w$. Equation (8) is the extension of Eqs. (6) and (7) to any distance w using the most likely path $\hat{\boldsymbol{\Gamma}}_i$ of proton i to interpolate intermediate positions between entrance and exit positions $\boldsymbol{x}_i^{in}$ and $\boldsymbol{x}_i^{out}$; it is indeed an interpolation process since $g_{j,p}(w^{out}) = g_{j,p}^{out}$ and $g_{j,p}(w^{in}) = g_{j,p}^{in}$. It was our hypothesis that accounting for the distance from the source to the binning plane allows improvement of the spatial resolution of objects located in that plane in the binned proton radiographs. This hypothesis has been validated in the first simulation.

In practice, $g_{j,p}$ is computed at a finite number of distances in the $\boldsymbol{w}$ direction, trilinear interpolation is used between the samples and we obtain a 4D sinogram $g : \mathbb{R}^3 \times \mathbf{P} \to \mathbb{R}$ instead of the conventional 3D sinogram, e.g., $g^{in}, g^{out} : \mathbb{R}^2 \times \mathbf{P} \to \mathbb{R}$. The optimal distance between samples $g_{j,p}$ in the $\boldsymbol{w}$ direction depends on the curvature of most likely paths, i.e., on the spatial straggling of protons due to multiple Coulomb scattering.

II.D. Distance-driven backprojection

The use of the distance-driven binning requires the modification of existing FBP algorithms. In this study, we adapted the Feldkamp–Davis–Kress (FDK) algorithm.[27] The 2D weighting and filtering of projection images in the FDK algorithm is not modified but repeated at every depth w; we note $\tilde{g}_p : \mathbb{R}^3 \to \mathbb{R}$ the filtered projection acquired at source position $\boldsymbol{a}_p$. A voxel-specific backprojection is used to select the adequate distance w, leading to the reconstruction formula

$$\eta(\boldsymbol{x}) = \sum_{p \in \mathbf{P}} \Delta\theta_p \left(\frac{\|\boldsymbol{o} - \boldsymbol{a}_p\|_2}{w(\boldsymbol{a}_p, \boldsymbol{x})}\right)^2 \times \tilde{g}_p\left(u(\boldsymbol{a}_p, \boldsymbol{x}), v(\boldsymbol{a}_p, \boldsymbol{x}), w(\boldsymbol{a}_p, \boldsymbol{x})\right) \tag{9}$$

with

$$\begin{cases} u(\boldsymbol{a}_p, \boldsymbol{x}) = \dfrac{w^{out}}{w(\boldsymbol{a}_p, \boldsymbol{x})}\left((\boldsymbol{x} - \boldsymbol{a}_p) \cdot \boldsymbol{u}(\boldsymbol{a}_p)\right), \\ v(\boldsymbol{a}_p, \boldsymbol{x}) = \dfrac{w^{out}}{w(\boldsymbol{a}_p, \boldsymbol{x})}\left((\boldsymbol{x} - \boldsymbol{a}_p) \cdot \boldsymbol{v}\right), \\ w(\boldsymbol{a}_p, \boldsymbol{x}) = (\boldsymbol{x} - \boldsymbol{a}_p) \cdot \boldsymbol{w}(\boldsymbol{a}_p), \end{cases}$$

and $\Delta\theta_p \in \mathbb{R}$ the angle weighting resulting from the discretization of the integral on the gantry angles. Equation (9) is similar to the standard FDK reconstruction formula except for the use of 3D projection images instead of 2D projection images where the last dimension is related to the distance to the source $w(\boldsymbol{a}_p, \boldsymbol{x})$. It is worth noting that both the backprojection and its FDK weighting depend on $w(\boldsymbol{a}_p, \boldsymbol{x})$.

The proposed algorithm is an approximate algorithm which takes advantage of improved spatial resolutions in proton radiographs during voxel-specific backprojection. One can observe that if the pixel indicators h were Dirac delta functions and if there was a single proton per indicator, using Eqs. (8) and (9) without filtering would simply backproject the proton energy integral G along the most likely proton path. The intermediate distance-driven binning is to allow the filtering of the FDK algorithm.

II.E. Simulations

The algorithm was implemented using RTK, an open-source reconstruction toolkit.[33] The evaluation was carried out on Monte Carlo simulations using GATE v6.2,[28] an end-user software using the Geant4 toolkit v4.9.5.p01.[29] Electromagnetic and hadronic interactions of primary and secondary protons were simulated, both in the air and in simulated objects. The `G4BraggModel` below 2 MeV and the `G4BetheBlochModel` beyond were used for inelastic electromagnetic interactions. The `G4UrbanMscModel95` described multiple scattering. Inelastic hadronic interactions with target nuclei were modeled using the `G4BinaryCascade` for protons with energies higher than 170 MeV, while the `G4PreCompound` was used for lower energies. Elastic hadronic interactions of protons were simulated with `G4HadronElastic`. The precalculated table of the stopping power and the particle range during Geant4 initialization were binned in the range of 0.1 keV to 10 GeV in a total number of 350 bins. The transportation step was 1 mm.

An ideal pCT scanner was simulated: a 200 MeV monoenergetic point source was placed at distance $\|\boldsymbol{o} - \boldsymbol{a}_p\| = 100$ cm from the isocenter and the characteristics (E_i^{in}, E_i^{out}, $\boldsymbol{x}_i^{in}$, $\dot{\boldsymbol{x}}_i^{in}$, $\boldsymbol{x}_i^{out}$, and $\dot{\boldsymbol{x}}_i^{out}$) of protons traversing the planes $w^{in} = 89$ cm and $w^{out} = 111$ cm were recorded. The measurements were exact, i.e., assumed perfect detectors, and the envelope Ω of each scanned object was also assumed to be perfectly known.

Standard 3σ cuts on energy and angle were applied to discard secondary protons produced by nuclear interactions.[24] Since it is not possible to measure in reality the exact path of each proton, the most likely path of each proton was estimated using its characteristics (position, direction, and energy) recorded at each of the two detectors. We used straight paths outside Ω and curved paths in Ω according to the maximum likelihood formalism of Schulte *et al.*[14] We closely followed their work for the parametrization of the estimation of the most likely paths.

The simulations used the materials properties defined in Geant4 based on the databases of the *National Institute of Standards and Technology* (NIST), including modifications with respect to NIST based on experiments, e.g., I_{H_2O} which equals 78 eV instead of 75 eV since Geant4 v4.9.3. In both Eq. (3) and the most likely path estimation, the object was assumed to be homogeneous and made of water. The energy integral G [Eq. (3)] was computed numerically with 100 eV bins.

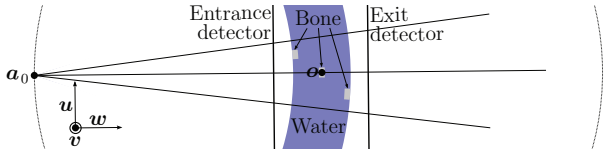

FIG. 2. Drawing of the setup of simulation 1.

II.E.1. Simulation 1

The first simulation was designed to provide the reader with insights into the effect of the distance-driven binning by looking at a single projection image only, i.e., $P = 1$. We centered a spherical shell of water with radii 90 and 110 cm around the proton source, therefore placing the isocenter in the middle of the water layer (Fig. 2). Three spherical bone inserts with identical solid angles were placed in the water sphere with regular radii from the source ($90 - 92$, $99 - 101$, and $108 - 110$ cm). Since all objects are portions of hollow spheres centered on the source position $\boldsymbol{a}_1$, the projection image for particles travelling along straight lines crossing the source would be a rectangular function with one rectangle per insert. The flux of protons through the plane $(\boldsymbol{o}, \boldsymbol{w})$ was uniform and equal to 648 000 protons $\cdot$ mm^{-2}, allowing distance-driven binning in a fine lattice with $0.1 \times 2 \times 0.1$ mm^3 spacing of $2500 \times 1 \times 2500$ samples in the $\{\boldsymbol{u}, \boldsymbol{v}, \boldsymbol{w}\}$ coordinate system.

II.E.2. Simulation 2

The second simulation was designed to measure the spatial resolution in reconstructed images relative to the depth of inserts in the object. Several aluminium cylinders with ø5 mm were regularly placed along a spiral in a large water cylinder with ø20 cm (Fig. 3). The total flux of protons was equal to the one of simulation 1 but $P = 720$ projection images were simulated which gave a proton flux of 900 protons $\cdot$ mm^{-2} $\cdot$ projection^{-1}. The projection images were binned in a lattice with $0.5 \times 1 \times 0.5$ mm^3 spacing of $500 \times 2 \times 500$ samples. Only the central slice $(\boldsymbol{o}, \boldsymbol{v})$ of the pCT image was reconstructed to avoid the cone-beam artifacts which are only encountered in other slices and depend on the scanned object.[27,30] The resolution of reconstructed images was $2100 \times 1 \times 2100$ voxels with 0.1 mm isotropic spacing. In addition to the proposed reconstruction formula [Eq. (9)], the standard FDK algorithm was used with the sinograms binned before ($w = 90$ cm) and after ($w = 110$ cm) the objects, respectively.

II.E.3. Simulation 3

The third phantom is a phantom used to measure the spatial resolution of clinical CT scanners, the CTP528 high-resolution module of the Catphan phantom (The Phantom Laboratory, Salem, NY). The module consists in various resolution gauges made of 2 mm-thick aluminium sheets placed on a ø10 cm circle in a ø20 cm water cylinder (Fig. 4). The parameters were the same as the ones of simulation 2.

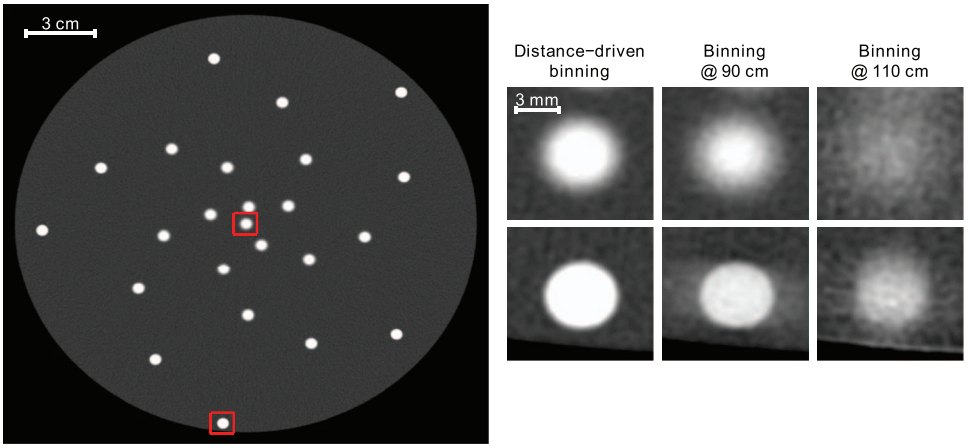

FIG. 3. Simulation 2. Central slice of the pCT reconstruction with distance-driven binning (left) and zooms on the central (right, top line) and peripheric (right, bottom line) inserts indicated with squared boxes. Gray-level range: [0.7, 2]. The first column of zoomed images were obtained with the proposed algorithm and the second and third columns were obtained with the standard FDK algorithm using sinograms binned according to the position of protons at 90 cm (entrance of the phantom) and 110 cm (exit of the phantom) from the source, respectively.

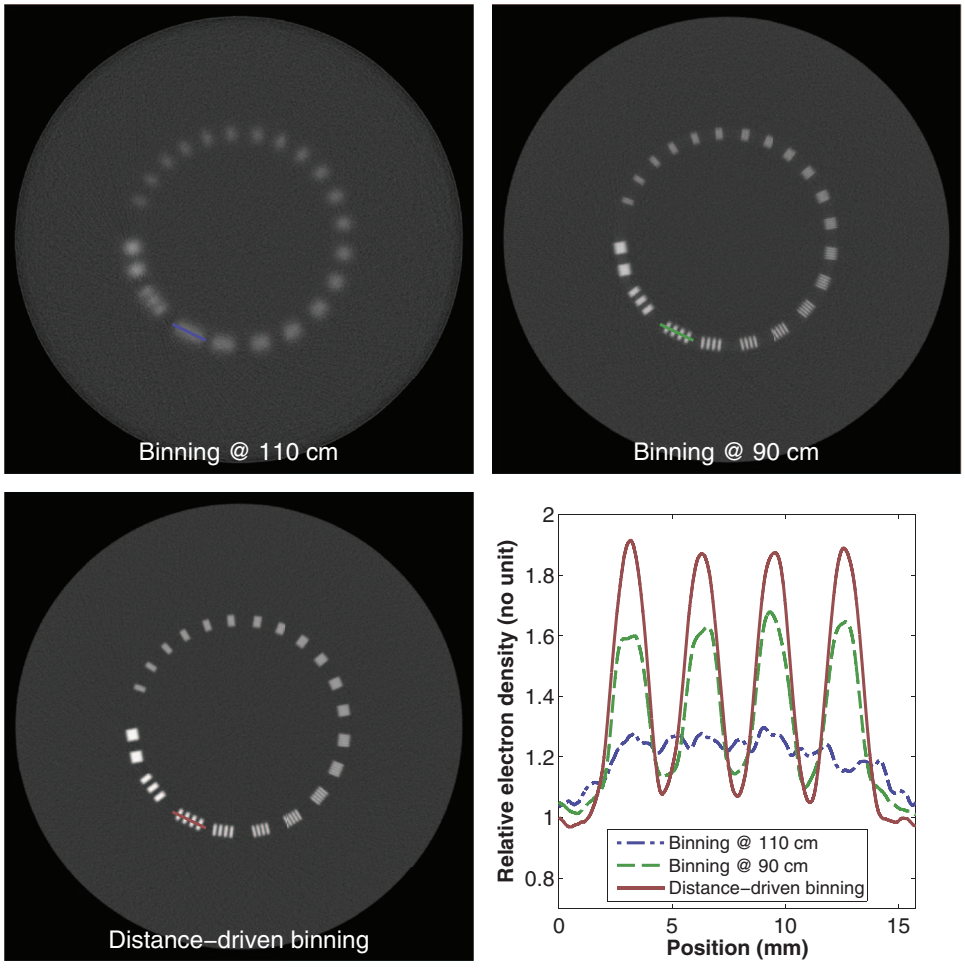

FIG. 4. Simulation 3, full scan. (Top-left) central axial slice of the standard FDK reconstruction using the 2D set of projection images $g(110\,\text{cm})$ binned according to the position of protons at the exit of the object. Gray-level range: [0.7, 2]. (Top-right) idem with the sinogram $g(90\,\text{cm})$ at the entrance of the object. (Bottom-left) distance-driven FDK reconstruction using the complete set of 3D projections g. (Bottom-right) profile along the three segments drawn on each slice.

II.E.4. Spatial resolution

The spatial resolution was quantified by measuring the edge response of the inserts with the distance required for the edge response to rise from 10% to 90%.[31] Higher values mean lower spatial resolution.

III. RESULTS

III.A. Simulation 1

Figure 5 illustrates the distance-driven binning in the projection space. The effect of multiple Coulomb scattering depended on the distance to the source and the position of the inserts. The edges of the bone inserts were the sharpest at the distance w in the sinogram which corresponds to their location in space, i.e., at the level of each line profile (Fig. 5, bottom). The loss of sharpness increased with the distance to their location (Fig. 5, right). The best spatial resolution was obtained for the right insert, which was the closest to the entrance, whereas the worst spatial resolution was obtained for the middle insert which is the one at the isocenter. This is related to the performances of the most likely path estimation, illustrated with the 3σ error envelope (Fig. 5, top-right, dashed curve) which increases with depth in the object, the increase being higher on the exit side ($w < 1000$ mm) than on the entrance side ($w > 1000$ mm). η for water and bone are 1 and 1.77, respectively, so the minimum and maximum of the profiles should be 200 and 215.3 mm [Eq. (3)]. The minimum is accurate but the maximum is slightly underestimated due to the use of the $I_{H_2O} = 78$ eV ionization potential of water instead of the $I_{Bone} = 92$ eV ionization potential of bone.

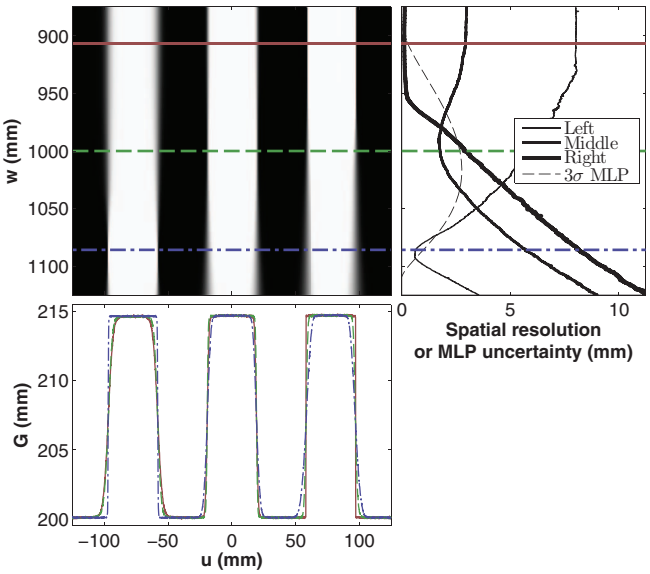

FIG. 5. Simulation 1. 2D slice of the binned 3D projection image (top-left) with the three profiles at the distance corresponding to the center of each insert (bottom-left) and the 10%–90% distance of each insert relative to the distance w to quantify the spatial resolution (top-right, solid lines). The top-right plot also displays the 3σ uncertainty of the MLP of protons with entrance and exit positions and directions along the central ray $\boldsymbol{a}_p\boldsymbol{o}$ (dashed line) computed using Eq. (27) of Schulte's derivation of the most likely path (Ref. 14). The 10%–90% distance was measured on each side of the inserts but the minimum of the two distances is plotted for each insert. The right, middle and left inserts are located at $90-92$, $99-101$, and $108-110$ cm from the source, respectively.

III.B. Simulation 2

The spatial resolution in the reconstructed pCT images can be visually observed in Fig. 3. The spatial resolution was not spatially uniform and gradually degrading from the periphery to the center of the phantom. Zooms on two pCT images reconstructed with the standard FDK algorithms are provided for comparison. The binning $g(110\,\text{cm})$, which uses the positions of protons after the object as provided by proton radiographs, gives the worst spatial resolution. The binning $g(90\,\text{cm})$, which uses the position of protons before the object, improves the spatial resolution but the distance-driven binning g [Eq. (8)] with the proposed reconstruction formula [Eq. (9)] was visually better.

The depth-dependence and the improved spatial resolution were quantified by looking at the 10%–90% distance of the edge profile of each aluminium insert (Fig. 6). Each 4 mm profile was obtained by averaging 360 radial profiles with equal angular spacing taken from the center of each insert. The range of spatial resolutions were $0.7-1.6$, $1.0-2.4$, and $2.2-3.2$ mm for the distance-driven binning, the binning $g(90\,\text{cm})$ and the binning $g(110\,\text{cm})$, respectively. Note that the inserts were not large enough for accurately measuring spatial resolutions greater than 1.5 mm due to the influence of the opposite side, which explains the noisy pattern of, e.g., $g(110\,\text{cm})$. The relative electron density η was accurately reconstructed for water ($\eta_{H_2O} = 1$) but that of aluminium was underestimated ($\eta_{Al} = 2.34$), probably because of the ionization potential assumption in Eq. (3) ($I_{Al} = 166$ eV).

III.C. Simulation 3

The improvement on spatial resolution was confirmed using simulations of a real phantom designed to measure the spatial resolution of photon CT scanners (Fig. 4). Profiles are provided through the pattern corresponding to $3\,\text{lp}\cdot\text{cm}^{-1}$. The spatial resolution improved with the distance binning compared to the spatial resolution of reconstruction using the original FDK algorithm with binning using the proton positions before and after the object (Fig. 4, bottom left vs two top slices). Among the two reconstructions with the original FDK algorithm, the binning before the object had a better spatial resolution.

The effect is emphasized when only a subset of projection images is used which corresponds to a short scan (Fig. 7). Parker weighting[32] was used to account for the short scan in each reconstruction of Fig. 7.

IV. DISCUSSION

We have proposed an algorithm to use curved most likely paths in a pCT filtered backprojection algorithm [Eq. (9)]. Our

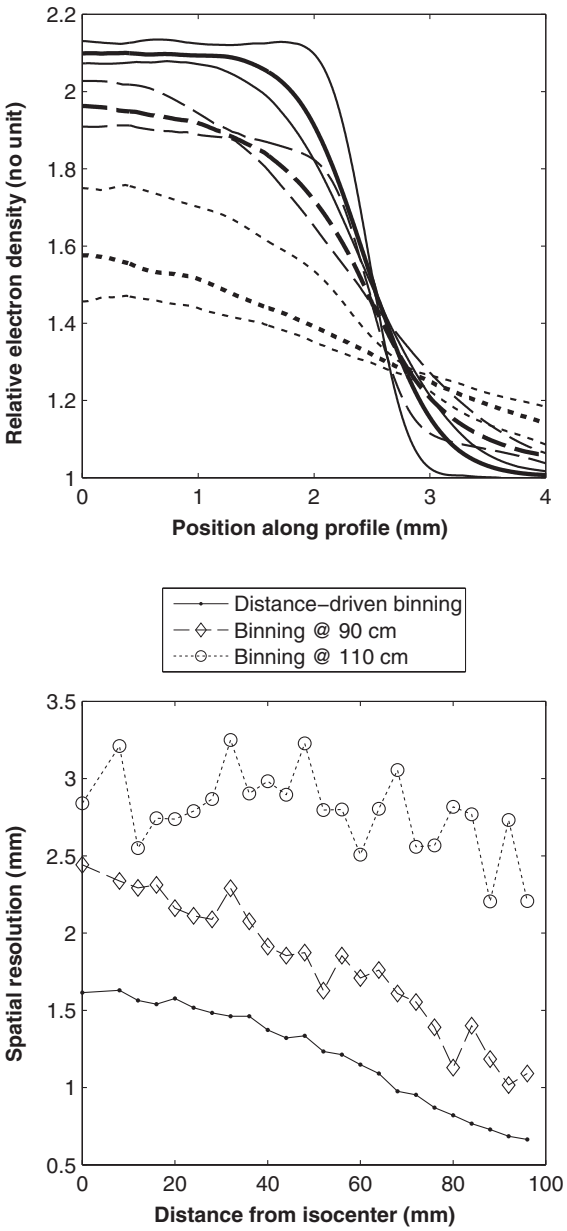

FIG. 6. Simulation 2. Quantification of the spatial resolution of each insert of Fig. 3. (Top) median (thick line) and 5/95-centile (thin lines) of the 24 average profiles. (Bottom) spatial resolution quantified with the 10%–90% distance of the edge profile of each edge insert relatively to the insert distance to the isocenter.

solution uses a distance driven binning in order to improve the spatial resolution in proton radiographs (Fig. 2). During backprojection, the spatial position of each voxel is translated to a distance to the source and the corresponding radiograph in the binned radiographs is used so that the sharpest binning is selected for objects at the voxel location. The improvement of the spatial resolution in projection images is propagated to the reconstructed pCT images and substantial improvement has been observed compared to other pCT images reconstructed with the original FDK algorithm (Figs. 3, 4, 6, and 7).

A side observation of this study is that existing FBP algorithms are more efficient with binning using proton positions before they enter the scanned object than proton positions after they exit the scanned object, the latter binning corresponding to what is obtained with real proton radiographs without proton tracking before the exit detector.[2] This difference is due to the higher energy of protons before they enter the object: since the effect of multiple Coulomb scattering increases with energy loss, the difference between their path and a straight line will gradually increase and the exit position is the worst position to estimate the straight line.[11] The substantial improvement obtained by tracking the protons before the object might be sufficient in some cases, for example, when the observed inserts are not at the center of the object and a full scan is performed, as is the case in Fig. 4. If the improvement is not sufficient or if short scan acquisitions are used, our algorithm further increases the spatial resolution at the cost of a tracking detector after the scanned object in addition to the detector for measuring the residual energy (Fig. 1).

Several choices have been made in the implementation of the proposed algorithm which could be modified to further improve the image quality. First, we have used voxel indicators for the binning [Eq. (5)] but more advanced basis functions could be used to allow, e.g., bilinear splitting during binning. Another potential improvement is the use of more robust estimators than the average during binning [Eq. (8)], e.g., the median, to eliminate outliers such as protons which underwent hadronic collisions. Finally, we could also allow binning of one proton through several source positions as it has been proposed in the parallel geometry.[21] These potential improvements have, however, a computational cost which was deemed prohibitive in the context of this study where a high proton flux was used. They might be required in the context of low dose pCT. Faster reconstruction could also be obtained by tuning the spacing of the samples of the distance-driven binning in the $\boldsymbol{w}$ direction. We have used the same spacing as in the $\boldsymbol{u}$ direction, to enforce fine sampling of the most likely path, but the spacing could be optimized to reduce computational cost (Fig. 2)

This FBP algorithm is as approximate as other FBP algorithms used in pCT since there is no exact solution for curved trajectories. We observed an improved spatial resolution without apparent loss in density resolution (Figs. 3 and 4) because the algorithm only modifies high frequencies of the sinogram without modifying low frequencies (Fig. 5). The algorithm is inspired by our experience in approximate motion compensated FBP reconstruction where limited differences have been observed with iterative reconstruction.[19] In the future, we intend to compare the proposed algorithm with existing pCT iterative algorithms to study their relative performances in terms of spatial and density resolutions at several levels of imaging doses.

It has been reported that FBP algorithms provide good density resolution compared to iterative algorithms such as algebraic reconstruction algorithms.[21] In our simulations, we observed that the electron density of water was accurately reconstructed but the electron density of aluminum inserts was systematically underestimated (Figs. 3 and 4). We believe that

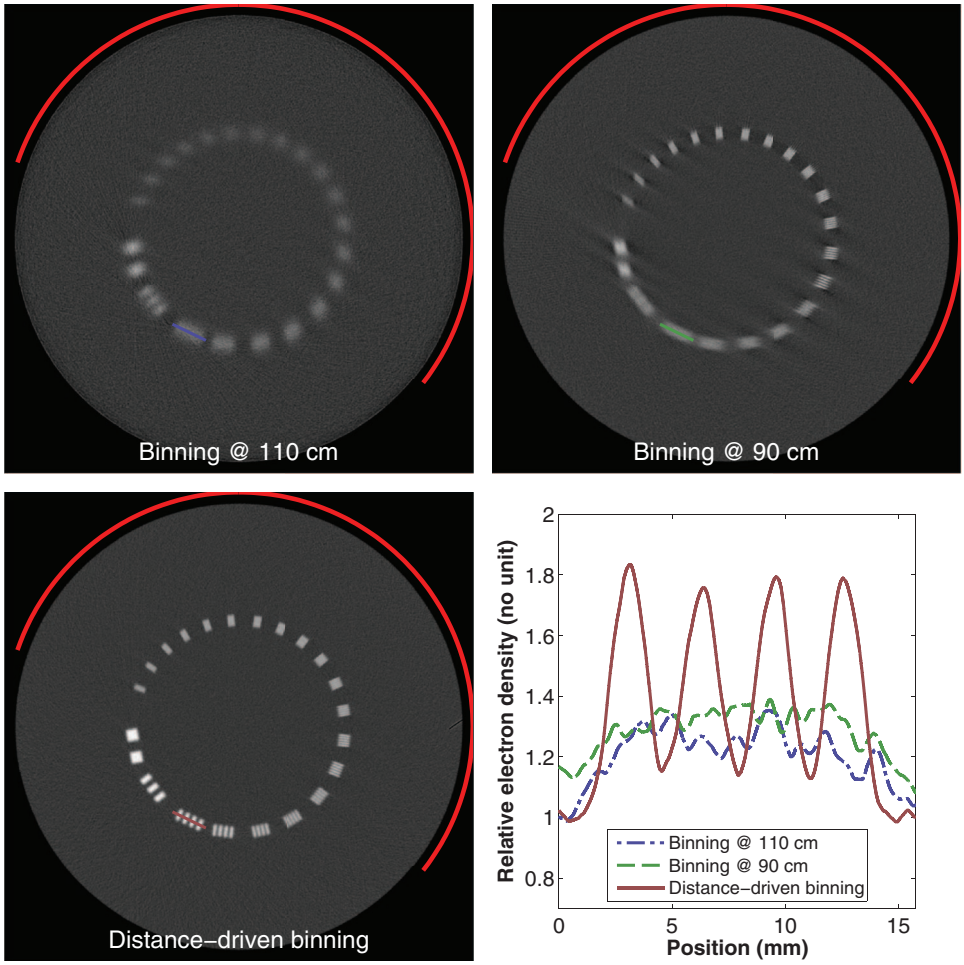

FIG. 7. Simulation 3, short scan. Idem as Fig. 4 with an additional circle arc indicating the angular coverage of the source trajectory with a down-scaled diameter for illustration purposes (ø20.5 cm on the figure instead of ø200 cm in reality).

the approximation of the ionization potential to that of water in Eq. (2) is the cause of this inaccuracy since the problem already arises in the projection space in simulation 1. We are currently investigating this with an extensive study on density resolution, also including the simulation of more realistic beam lines and detectors.

The phantoms simulated in this study were almost homogeneous and essentially made of water. These properties have been used in the most likely path estimation as in many past studies on pCT, but are unrealistic for patient imaging. We have planned on evaluating the impact of assuming an homogeneous target on the spatial resolution of patient pCT images. If inhomogeneities were prohibitively degrading spatial resolution, they could still be accounted for in Schulte's bayesian framework[14] using, e.g., a first pCT image reconstructed without most likely path estimation to roughly estimate the tissues map.

The major advantage of our algorithm over iterative pCT algorithms is faster on-the-fly reconstruction. These assets could become essential for their use in proton therapy treatment rooms when the reconstructed image is required to check the patient anatomy prior to starting the treatment. In this context, a short scan could also potentially reduce the acquisition time and the imaging dose, for which the use of most likely paths seems crucial (Fig. 7).

V. CONCLUSION

We have developed a filtered-backprojection pCT reconstruction algorithm that takes advantage of the estimation of the most likely path of protons. Improvement in the spatial resolution has been observed on Monte Carlo simulations compared to existing straight-line approximations. The improvement in spatial resolution combined with the practicality of FBP algorithms compared to iterative reconstruction algorithms makes this new algorithm a candidate of choice for clinical pCT.

ACKNOWLEDGMENTS

This work was supported by the grant ProTom (ITMO Cancer et Technologie in the Plan Cancer 2009–2013 program), the LabEX PRIMES (ANR) and the Lyric grant INCa-4664.

[a]Author to whom correspondence should be addressed. Electronic mail: simon.rit@creatis.insa-lyon.fr

[1]A. Cormack, "Representation of a function by its line integrals, with some radiological applications," J. Appl. Phys. **34**, 2722–2727 (1963).
[2]U. Schneider *et al*., "First proton radiography of an animal patient," Med. Phys. **31**, 1046–1051 (2004).
[3]R. Schulte *et al*., "Conceptual design of a proton computed tomography system for applications in proton radiation therapy," IEEE Trans. Nucl. Sci. **51**, 866–872 (2004).
[4]V. Sipala *et al*., "PRIMA: An apparatus for medical application," Nucl. Instrum. Methods Phys. Res. A **658**, 73–77 (2011).
[5]B. Schaffner and E. Pedroni, "The precision of proton range calculations in proton radiotherapy treatment planning: Experimental verification of the relation between CT-HU and proton stopping power," Phys. Med. Biol. **43**, 1579–1592 (1998).
[6]M. Yang *et al*., "Comprehensive analysis of proton range uncertainties related to patient stopping-power-ratio estimation using the stoichiometric calibration," Phys. Med. Biol. **57**, 4095–4115 (2012).
[7]H. Paganetti, "Range uncertainties in proton therapy and the role of Monte Carlo simulations," Phys. Med. Biol. **57**, R99–117 (2012).
[8]G. Cirrone *et al*., "Monte Carlo evaluation of the filtered back projection method for image reconstruction in proton computed tomography," Nucl. Instrum. Methods Phys. Res. A **658**, 78–83 (2011).
[9]D. Wang *et al*., "Bragg peak prediction from quantitative proton computed tomography using different path estimates," Phys. Med. Biol. **56**, 587–599 (2011).
[10]N. Depauw and J. Seco, "Sensitivity study of proton radiography and comparison with kV and MV x-ray imaging using Geant4 Monte Carlo simulations," Phys. Med. Biol. **56**, 2407–2421 (2011).
[11]U. Schneider and E. Pedroni, "Multiple Coulomb scattering and spatial resolution in proton radiography," Med. Phys. **21**, 1657–1663 (1994).
[12]H.-W. Sadrozinski *et al*., "Development of a head scanner for proton CT," Nucl. Instrum. Methods Phys. Res. A **699**, 205–210 (2013).
[13]D. Williams, "The most likely path of an energetic charged particle through a uniform medium," Phys. Med. Biol. **49**, 2899–2911 (2004).
[14]R. W. Schulte *et al*., "A maximum likelihood proton path formalism for application in proton computed tomography," Med. Phys. **35**, 4849–4856 (2008).
[15]B. Erdelyi, "A comprehensive study of the most likely path formalism for proton-computed tomography," Phys Med Biol **54**, 6095–6122 (2009).
[16]A. Katsevich, "An accurate approximate algorithm for motion compensation in two-dimensional tomography," Inverse Probl. **26**, 065007 (2010).
[17]L. Desbat *et al*., "Compensation of some time dependent deformations in tomography," IEEE Trans. Med. Imaging **26**, 261–269 (2007).
[18]C. Ritchie *et al*., "Correction of computed tomography motion artifacts using pixel-specific back-projection," IEEE Trans. Med. Imaging **15**, 333–342 (1996).
[19]S. Rit *et al*., "Comparison of analytic and algebraic methods for motion-compensated cone-beam CT reconstruction of the thorax," IEEE Trans. Med. Imaging **28**, 1513–1525 (2009).
[20]T. Li *et al*., "Reconstruction for proton computed tomography by tracing proton trajectories: A Monte Carlo study," Med. Phys. **33**, 699–706 (2006).
[21]S. Penfold, "Image reconstruction and Monte Carlo simulations in the development of proton computed tomography for applications in proton radiation therapy," Ph.D. thesis, Centre for Medical Radiation Physics, University of Wollongong, 2010.
[22]S. Rit *et al*., "On-the-fly motion-compensated cone-beam CT using an a priori model of the respiratory motion," Med. Phys. **36**, 2283–2296 (2009).
[23]J. Beringer *et al*. (Particle Data Group), "Review of particle physics," Phys. Rev. **D86**, 010001 (2012).
[24]R. Schulte *et al*., "Density resolution of proton computed tomography," Med. Phys. **32**, 1035–1046 (2005).
[25]K. Hanson *et al*., "Computed tomography using proton energy loss," Phys. Med. Biol. **26**, 965–983 (1981).
[26]P. Zygmanski *et al*., "The measurement of proton stopping power using proton-cone-beam computed tomography," Phys. Med. Biol. **45**, 511–528 (2000).
[27]L. Feldkamp *et al*., "Practical cone-beam algorithm," J. Opt. Soc. Am. A **1**, 612–619 (1984).
[28]S. Jan *et al*., "GATE V6: A major enhancement of the GATE simulation platform enabling modelling of CT and radiotherapy," Phys. Med. Biol. **56**, 881–901 (2011).
[29]S. Agostinelli *et al*., "Geant4-a simulation toolkit," Nucl. Instrum. Methods Phys. Res. A **506**, 250–303 (2003).
[30]S. Mori *et al*., "Properties of the prototype 256-row (cone beam) CT scanner," Eur. Radiol. **16**, 2100–2108 (2006).
[31]S. W. Smith, *The Scientist and Engineer's Guide to Digital Signal Processing* (California Technical Publishing, San Diego, CA, 1997).
[32]D. Parker, "Optimal short scan convolution reconstruction for fanbeam CT," Med. Phys. **9**, 254–257 (1982).
[33]See http://www.openrtk.org for recontruction toolkit (RTK).